Propagation speeds of strongly nonlinear near-surface internal waves in the Strait of Georgia

C. Wang[1,2] and R. Pawlowicz[1]

Received 10 November 2010; revised 6 July 2011; accepted 22 July 2011; published 15 October 2011.

[1] A novel aerial observational method for studying internal features in the coastal ocean is developed and tested in a study of large nonlinear internal solitary-like waves. Photogrammetrically rectified oblique photo images from a circling aircraft are used to track a number of internal wave packets for periods of up to one hour in the Strait of Georgia, British Columbia, Canada. Combining these sequences with coincident water column data allows us to obtain a more complete view of the spatial structure of internal waves. Highly accurate measurements of wave propagation speeds and directions are possible. The applicability of various weakly nonlinear theories in modeling propagation of the observed large-amplitude waves is tested. The measured wave speeds enable us to differentiate between classic internal wave models. The linear, KdV (Korteweg-de Vries), and BO (Benjamin-Ono) models are applied with and without background shear. After background shear effects are included, it is found that a continuously stratified BO equation can predict propagation speeds within observational error, and that this is not true for other theories. The technique may be useful in future studies of oblique internal wave interactions.

Citation: Wang, C., and R. Pawlowicz (2011), Propagation speeds of strongly nonlinear near-surface internal waves in the Strait of Georgia, *J. Geophys. Res.*, *116*, C10021, doi:10.1029/2010JC006776.

1. Introduction

[2] Internal waves are a widespread geophysical phenomenon in stratified fluids. They exist in coastal seas, straits, fjords, continental shelves, lakes, and the atmospheric boundary layer, and are created by a large variety of forcing mechanisms [e.g., *Apel et al.*, 1995; *Helfrich and Melville*, 2006; *Helfrich and Grimshaw*, 2008]. When the wave amplitudes are very small, linear theory can satisfactorily predict their characteristics [*LeBlond and Mysak*, 1978]. However, in many cases the wave amplitudes are large enough that nonlinear effects become important in their dynamics. Waveform shapes will change and the propagation speeds tend to be larger than linear theory predicts. In addition, nonlinear waves exhibit a number characteristics (such as the existence of isolated pulses or solitary waves) that are not described by linear theory. Large amplitude internal waves can have a strong nonlinearity. As a consequence the waves steepen and break into rank ordered soliton trains. Nonhydrostatic dispersion then balances with the nonlinearity and the soliton waveform is preserved.

[3] At small but finite amplitudes, analytical theories of nonlinear waves are well-developed [*Helfrich and Melville*, 2006]. Isolated pulses in real fluids are often similar to so-called "soliton" solutions to these nonlinear dynamical equations. Laboratory experiments have verified many aspects of these soliton solutions in certain parameter ranges [e.g., *Ostrovsky and Stepanyants*, 2005; *Koop and Butler*, 1981], but some features (such as propagation speeds) have not been well studied. There are also many field observations of internal waves in the ocean. These rely on in-situ observations including conductivity-temperature-depth (CTD) profiles [e.g., *Klymak and Gregg*, 2004; *Moum et al.*, 2003], thermistor strings (T-chain) [e.g., *Marmorino*, 1987; *van Haren*, 2005], acoustic Doppler current profilers (ADCP) [e.g., *Moum et al.*, 2003; *Colosi et al.*, 2001], echo sounders [e.g., *Farmer and Armi*, 1999; *Moum et al.*, 2003], Doppler sonars [e.g., *Pinkel*, 1983], acoustic transceivers [e.g., *Dushaw et al.*, 1995], bathythermographs [e.g., *Wijffels and Meyers*, 2004], Lagrangian floats [*D'Asaro*, 2003; *Centurioni*, 2010], inverted echo sounders (IES) [*Li et al.*, 2009], and wirewalkers [*Pinkel et al.*, 2011]. However, these data sets are usually not well-suited for making precise measurements of propagation speed and direction. It is not clear, for example, if repeated transects or horizontally separated moorings resample the same part of a wavefront, or if their locations are shifted laterally along the wave crests, or indeed if the same wavefront is being sampled since wave-wave interactions may have occurred between the discrete observations. Some studies have used large collections of moored instruments to study the evolution in time and space [*Ramp et al.*, 2004], but determining the true direction of propagation and the evolution during the time the wave travels between moorings is rather complicated.

[4] More direct wavefront observations, from which propagation characteristics can be inferred, can sometimes be made by exploiting a well-known phenomenon in which

[1]Department of Earth and Ocean Sciences, University of British Columbia, Vancouver, British Columbia, Canada.
[2]Now at Physical Oceanography Laboratory, Ocean University of China, China.

0148-0227/11/2010JC006776

near-surface internal waves affect the roughness of the water surface. These roughness changes result in banded changes in the color and shade of the surface when viewed obliquely at a distance. The interaction between surface waves and a spatially varying current induced by the internal wave can account for the presence of both smooth and rough bands [*Gargett and Hughes*, 1972]. In an internal wave of depression in an approximately two-layer water system where the upper layer is much thinner than the lower layer, the surface at the leading edge of the wave is much rougher due to convergence and downwelling. On the other hand, at the trailing edge, the upper layer water is upwelling and diverging, and the water surface is smoother. When viewed at highly oblique angles the surface reflectance dominates the optical characteristics of light traveling outward from the surface. The visible light reflected in these neighboring regions then comes from different parts of the sky, which is not uniformly lit, and hence they appear as contrasting bands, darker or lighter than surrounding surface waters. Contrasting roughness bands may also result in different responses to radar pulses.

[5] These banding features of the water surface can be captured by remote sensing equipment which operates at oblique angles, such as synthetic aperture radar (SAR), or as in this paper, optical imaging with a handheld camera. Photographic methods have a long history. Some of the earliest photographic observations of internal wave slicks were made in the Strait of Georgia, British Columbia, Canada [*Shand*, 1953; *Turner*, 1973], where the internal waves are tidally generated by flow through neighboring sills and channels [*Gargett*, 1976]. This region has also been the site of SAR studies of internal waves [e.g., *Hughes and Gasparovic*, 1988]. Space-based remote sensing techniques provide data over a wide area but have the disadvantage that it is almost impossible to repeatedly observe the same wave packet over short period of time. On the other hand, photographic techniques are ideally suited to repeatedly imaging these features over short time periods.

[6] Oblique digital photography has been previously used from helicopters [*Farmer and Armi*, 1999; *Cummins et al.*, 2003], as well as from fixed shore locations [*Cummins et al.*, 2003; *Pawlowicz*, 2003; *Bourgault*, 2007]. Time sequences of photogrammetrically rectified images from shore stations have been derived for quantitative analysis, but aerial photography has only been used qualitatively. Unfortunately, although many regions of oceanographic interest are not situated close to a convenient hilltop, adapting the photogrammetric techniques developed for fixed shore stations for use on a rapidly moving platform introduces a number of difficulties. Vertical motions and sharp turns cause the view point to change rapidly, and optical measurements are often quite sensitive to these variations. In addition, the lack of spatial references from (say) trees or nearby coastlines can make geometrical adjustments more difficult. Here it is shown that these difficulties can be overcome in some practical situations, so that quantitative results can be obtained.

[7] In this paper, we discuss observations of near-surface internal waves in the Strait of Georgia. Combined aerial and water column observations were made over a period of several months, so that a wide variety of conditions were observed. Using oblique aerial photography, the propagation speeds of uniquely identified internal wave crests, far enough apart that they do not interact with other waves over the time period of the study, are determined in a direction normal to their wavefronts. These waves are then considered to be "solitary", and hence their dynamics should be (approximately) described by soliton solutions to appropriate governing dynamical equations.

[8] The propagation speeds are then compared with predictions using various classical soliton theories. Although the wave amplitudes are very large, and are thus not strictly within the parameter range of these classical theories, it is shown that good predictions are made using soliton solutions to the Benjamin-Ono (BO) equation [*Benjamin*, 1966; *Ono*, 1975], but it is necessary to include both the effects of continuous stratification and background baroclinic shear in the mathematics. Other classical solutions, including the well-known Korteweg-de Vries (KdV) soliton, do not provide a satisfactory match with the observations, even when baroclinic shear and stratification effects are included. This work thus also represents the first field validation of the utility of the BO equation.

[9] In the next section, we describe the site of the study, and the methods used to obtain observations. We then discuss the form and propagation speeds of the waves observed. Finally, we compare the observations of wave propagation speeds with predictions made using a variety of analytical and semi-analytical theories of nonlinear wave propagation.

2. Method

2.1. Site

[10] The Strait of Georgia is a large marine waterway on the west coast of North America (Figure 1). It is partially enclosed by islands with Vancouver Island forming the western boundary, and a complex of small islands and channels marking its southern boundary. The Strait of Georgia is about 220 km long and 33 km wide with an average depth of 150 m, but with a small fraction of the total area exceeding 350 m in depth. Depths in the regions observed in this study are greater than 120 m.

[11] The tide has a maximum range exceeding 4 m in the Strait. Although tidal currents can be greater than 1 m s^{-1} in some of the constricted southern passages, they are generally no more than a few 10 s of cm s^{-1} within the Strait itself [*Foreman et al.*, 1995].

[12] Stratification is typical for fjord-type estuaries, with a large density gradient near the surface, little or no uniform mixed layer, and relatively weak stratification at depth [*Pawlowicz et al.*, 2007]. The main source of freshwater maintaining this stratification is the Fraser River. This river discharges near the main entrance of the Strait of Georgia and its turbid plume dominates the southern strait especially in late spring and early summer [*Halverson and Pawlowicz*, 2008]. However, our observations were generally taken away from the direct influence of the plume.

[13] Many internal waves in the Strait of Georgia are concentrated near the surface, with maximum depressions of as much as 7 m for isopycnals whose undisturbed depth, within the gradient between the surface brackish water and deep salty seawater is less than 5 m. The length scale (half wave width) across the wave crest is of order 50 m, and the

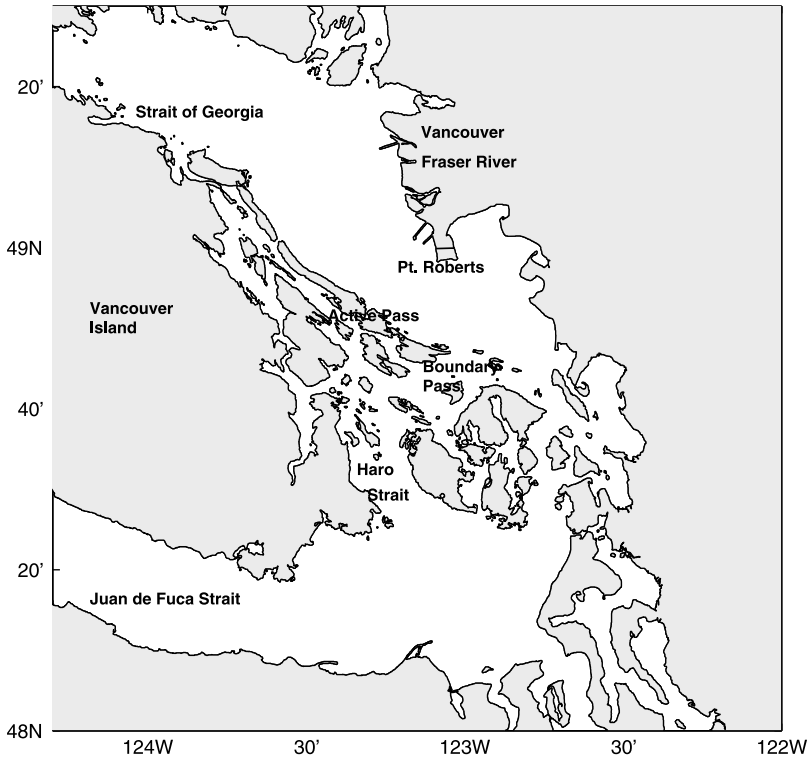

Figure 1. Map of the southern Strait of Georgia. The intensive field work for this paper research is carried out mostly in the region between Active Pass and Point Roberts.

wave crests themselves can sometimes stretch for 10–20 km across the Strait. It is this near-surface location that results in large near-surface currents, which, in turn, result in features regularly visible to the naked eye [*Shand*, 1953; *Turner*, 1973; *LeBlond and Mysak*, 1978]. This visibility is enhanced by the relatively calm and sunny conditions that often occur for periods of several days within the Strait during summer, separated by short periods of more windy conditions in which the internal wave surface features cannot be reliably viewed. Thus, the Strait of Georgia is a useful natural laboratory for studying internal waves using optical techniques.

[14] Preliminary aerial reconnaissance in 2001 suggested that internal waves could reliably be found between Active Pass and Point Roberts soon after times when the tidal amplitude suggested low slack water. Field observations discussed in this paper were then obtained during 5 trips in the spring and summer of 2002 (May 24, June 3, June 10, June 25, and June 26) timed around low slack water. It was thought that internal wave amplitude might vary with the fortnightly variation in tidal amplitudes, which arises from tropic/equatorial variations related to lunar declination rather than spring/neap variations in the Strait (largest constituents are M2, followed by declinational constituents K1 and O1, with S2 being rather small [*Foreman et al.*, 1995]), and perhaps with the ambient stratification, which intensified during June as the freshet of the Fraser River peaks. Periods of both large and weak tides in relatively calm conditions were sampled, both before and during the freshet. From this data set, 13 individual waves were analyzed. The waves chosen appeared to be far enough apart from other waves (either from the same wave packet or from other wave packets) so that no wave-wave interactions were occurring, and thus can be treated as "solitary-like" waves.

2.2. Observations

[15] The primary observational data set are time sequences of geographically located oblique aerial images (e.g., Figure 2) with known aiming direction. These were obtained using a single-engine 4-passenger floatplane. However, these sequences were interpreted with the aid of simultaneous water column measurements, made within the field of view of the images. These water column measurements include time-synchronized in-water CTD, ADCP, echo sounder, and T-chain measurements. Water column measurements were obtained from instruments mounted on a hovercraft (the Canadian Coast Guard Hovercraft *Siyay*).

[16] Coordinated sampling was achieved by identifying a suitable internal wave packet from the aircraft, and then directing the hovercraft to a location immediately ahead of the wave crest. This could be done relatively quickly in spite of the distances involved (10 s of km) because of the high speeds (>40 knots) possible with the hovercraft. Once in place, the hovercraft then went into a "boating" mode in which instruments were deployed into the water column, and the hovercraft driven across the wavefronts. A disadvantage of "boating" is that the vessel speed is limited to only a few knots, occasionally causing the vessel to be temporarily trapped in the surface convergence field. This degraded the quality of echo soundings and T-chain data. Maximum displacements can be reliably determined but waveshapes are often distorted.

[17] The instruments used include a 300 kHz RD Instruments Workhorse "Sentinel" ADCP, and a 100 kHz echo

Figure 2. An image of internal wave slicks near Active Pass looking south on June 26, 2002. The hovercraft *Siyay* providing water column data is the dark object at center right. The labels "1st", "2nd", and "3rd" denote the same three waves as in Figures 3 and 4.

sounder, co-located on a mast deployed over the bow of the hovercraft. The ADCP had a velocity resolution of 1 mm s^{-1} and an accuracy of ±1 cm s^{-1}. Density profiles were obtained using a Seabird Electronics SBE25 CTD. In addition, vertical stratification was monitored by deploying a chain of thermistors deployed over the side of the hovercraft with temperature measured at nominal depths of 2, 3, 4, 5, 6, 8, 10, 12, 16, and 20 meters using RBR TR-1000 loggers with a response time of less than 1 second. The slow hovercraft transects tended to drag the chain so that it did not hang vertically. A RBR XL-200 temperature/pressure logger was therefore placed at 21 m to monitor the vertical position of the bottom of the chain. A Global Positioning System (GPS) receiver continuously monitored the hovercraft's position throughout the study. All instruments were time synchronized to within a few seconds.

[18] Ideal weather conditions for photo imaging are sunny and calm without many cloud shadows or rough surface waves. During a strait-wide survey, the altitude of the aircraft was as high as 1000 m to obtain a larger field of view, but during coordinated sampling with the hovercraft, the aircraft flew at an altitude of about 400 m and followed a square track several kilometers across, centered on the target area. This provides images at a dip angle of 5–10° (found to be optimal for seeing surface reflectance variations). A GPS recorded the track and altitude of the aircraft. The aiming direction of the handheld Kodak DC265 camera was monitored using a compass/tilt-meter attached to the base of the camera. Tilt-meter, GPS and the photo time stamp information were continuously and synchronously logged.

[19] Directional accuracy for the compass/tilt-meter was a few degrees in the absence of acceleration, but achieving this accuracy required some care as circling aircraft are capable of large accelerations. To aid in accurate rectification, the photo images were framed to include both the wave feature of interest and either the coastline, horizon and/or hovercraft to provide a known reference.

2.3. Rectification of Aerial Images

[20] A typical aerial oblique photograph (Figure 2) shows an apparently rank-ordered series of alternating light- and dark-colored bands. These raw photo images have to be rectified, photogrammetrically mapped to ground coordinates, and then processed using a series of filters and image processing tools into a base image (Figure 3) before quantitative analysis can be applied [*Pawlowicz*, 2003].

[21] A summary of the procedure is as follows. First, each pixel location is transformed into camera coordinates, identified as a view vector pointing from the center of the camera, relative to the camera axis. Second, this vector is transformed into earth coordinates with an origin at the camera location, using camera aiming direction information and altitude. Then, the relative intersection of this view vector with the ground plane is found. The curvature of the earth must be accounted for in this step. The ground point in earth coordinates will be the point at which a line extending from the origin in the view direction intersects the ground plane. Finally, the coordinates of the ground point relative to the camera are converted to true ground coordinates (latitude and longitude). In order to carry out these transformations, the latitude, longitude, and altitude of the camera/aircraft, three orientation angles (rotation, dip below horizon, and tilt around view axis), and camera parameters such as field of view are required. In addition to these geometrical transformations, other image processing was also applied to remove trees and land (when seen) and camera speckle. It was also useful to remove dark edges that arise from lens properties (so-called vignetting) by subtracting a fitted function of the camera focal length.

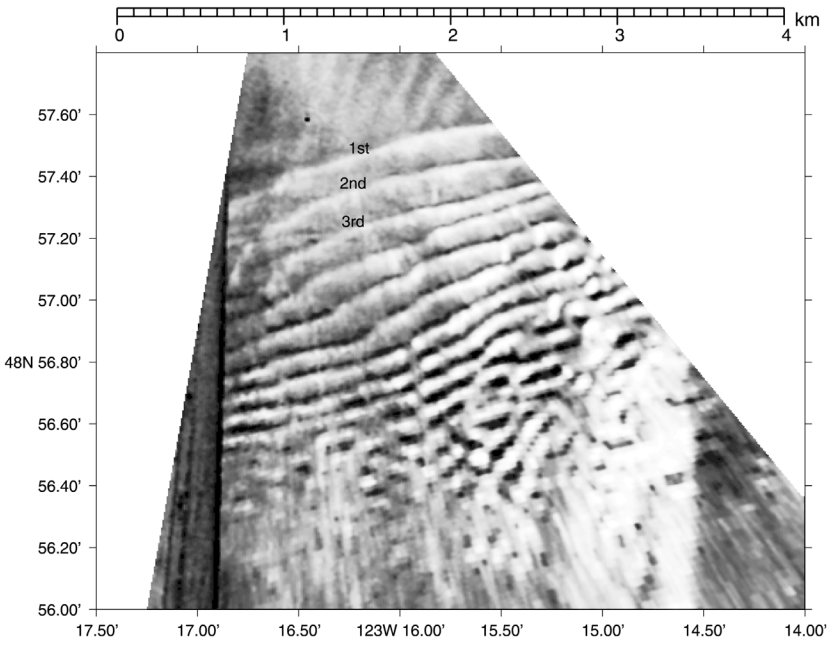

Figure 3. The wave packet observed around Active Pass on June 26, 2002. Original image can be found in Figure 2. Note that the leading six or so wave crests in the northern part of the image are far enough apart that they do not appear to be interacting with each other. However, the wave pattern is quite complex at the trailing end (southern) of the packet. The dark area at left is a wing of the airplane. Hovercraft *Siyay* is the black dot about 300 m ahead of the first wave. The labels "1st", "2nd", and "3rd" denote the same three waves as in Figures 2 and 4.

[22] Although the GPS measurements of the aircraft latitude and longitude are reasonably accurate, the orientation angles are sometimes not as precise as required, especially when the plane is changing altitude or making sharp turns, because the tilt-meter is sensitive to accelerations. The GPS altitude data stream is also somewhat prone to large jumps when the aircraft orientation is changing, and this required some manual corrections. The relative orientation of camera and tilt-meter varied from trip to trip due to mechanical variations in the attachment. Therefore, the recorded camera angles of tilt, rotation, and dip and the camera altitude had to be altered slightly by matching known locations and directions such as the coastlines and the position of the hovercraft before the photo images were successfully mapped. The average corrections of the three angles of tilt, rotation, and dip are 5°, 10°, and 3°, respectively. The tilt angles vary between −10° and 10°. The rotation angles range from 0° to 360°. The dip angles are around 6°. The corrections to the altitudes (when made) are about 50 m. The errors induced by all of the above result in an uncertainty in wave position, and their effects will be contained within the error bars estimated for derived characteristics.

[23] Measurements of propagation speed and direction are derived from photographic time sequences. Each time sequence lasts 15–30 minutes, with 1–2 images taken every minute. These sequences are short enough that background velocity and density fields remain relatively constant. During this period the waves propagate distances of 1–2 km. Wave locations are geographically located to within an uncertainty of less than 100 m, leading to uncertainties in the propagation speed of less than 10%. At the same time, tidal effects are obtained from coincident water column measurements and subtracted. Background density and baroclinic velocity fields are also determined.

3. Results

3.1. Wave Amplitudes

[24] Observable water column structure in both the echo sounder and ADCP data sets, associated with internal waves, was limited to the upper 20–30 m of the water column, which was generally deeper than 120 m. Displacements associated with internal waves were seen most cleanly in the echo sounder images (e.g., Figure 4). These displacements are seen by the vertical excursions of largely horizontal striations. As usual, the exact cause of such striations in echo sounder images is not well understood, but in the Strait of Georgia region they are thought to represent enhanced backscatter from locations where the fine-scale vertical density gradients are especially large [*Tedford et al.*, 2009]. Water parcels containing these gradients are then displaced vertically by the larger-scale internal wave motions.

[25] Wave amplitudes for the different waves in Figure 4 are similar. Because of the slow and irregular speed of the hovercraft in "boating" mode, the waveshapes (e.g., the "2nd" wave in Figure 4) appear somewhat irregular, and these irregularities may not represent real features. However, it is possible to compare the maximum depth of a horizontal striation against its "undisturbed" location to make relatively robust and accurate estimates of the maximum displacement. A similar process was applied to contours of T-chain data. Isotherms are taken as proxies for isopycnals. The displacement of isotherms in contour images made through the T-chain data matches the displacements of the horizontal

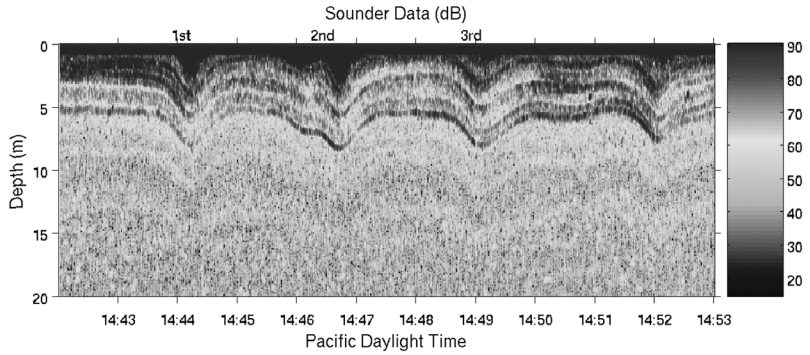

Figure 4. The in-water Sounder data of the wave packet observed near Active Pass on June 26, 2002. The labels "1st", "2nd", and "3rd" denote the same three waves as in Figures 2 and 3.

striations in the sounder image, but isotherms can also be located deeper in the water column. Isotherms near the surface and at depth have small displacements and an isotherm at some intermediate depth has the largest displacement. This maximum displacement for a particular wave was taken to be the wave amplitude.

[26] Observations sometimes suggested that the isopycnal depth after the wave passed was slightly different from that in front of the wave. This could occur either because the depth correction for the T-chain data was not completely accurate or due to asymmetries in the actual waveforms. In these cases, the average of the downward and upward displacements will be taken as the wave amplitude and the associated error bar (usually about 10 %) is the difference between the average and the two values. Measured wave amplitudes span a wide range, from 2.2 to 7.3 m (Figure 5), and the maximum displacement generally occurs at a depth of 2–5 m.

3.2. Stratification and Background Currents

[27] The density profiles obtained from CTD measurements near the waves analyzed in different days are summarized in Figure 6a. Largest density changes are confined in the upper 20 m, with most rapid decreases in the upper 5 m or so. Densities below 20 m remain almost uniform.

[28] The effects of background currents on internal wave propagation can be separated into those due to the barotropic or depth averaged currents and those due to the baroclinic currents. Waves are simply advected by the barotropic tide, whose effects are estimated by taking the depth average current. This advection is a translation with no dynamic relevance, but it affects the observations. In contrast, baroclinic currents in the water column can change the waveshape and speed. In both cases, the observed current is projected on the wave normal and only that component is used in modeling. Both the barotropic and baroclinic currents were obtained from segments of the data that did not include waves, i.e. either immediately before the leading wave of a packet or between waves.

[29] Baroclinic current profiles for different cases, obtained from ADCP data with the barotropic tide subtracted, are shown in Figure 6b. These profiles represent baroclinic currents in the direction of wave propagation. The downward-facing ADCP does not measure currents in the upper 1.5 m. The data are extrapolated by assuming that these currents are the same as the topmost measured value. Surface baroclinic currents are in the direction of wave propagation in some cases, and against the direction of propagation in others. In general, baroclinic currents are large near the surface and relatively small below 30 m. The maximum magnitude of baroclinic currents is less than 0.5 m s^{-1}, and usually less than 0.2 m s^{-1}, which implies that they are smaller than wave propagation speeds. Thus the complicating issue of critical layers [*Baines*, 1995] does not arise here.

[30] ADCP velocity profiles are contaminated by noise. In computing the effect of the vertical shear in the horizontal

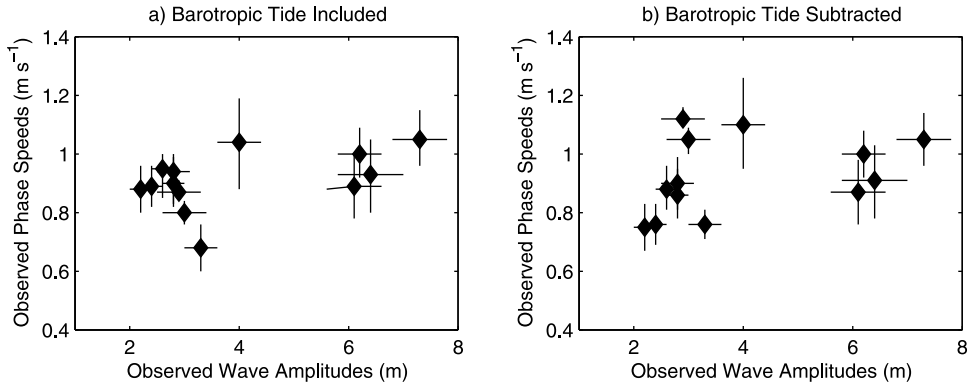

Figure 5. The observed wave amplitudes and wave phase speeds (a) before and (b) after barotropic tide is removed.

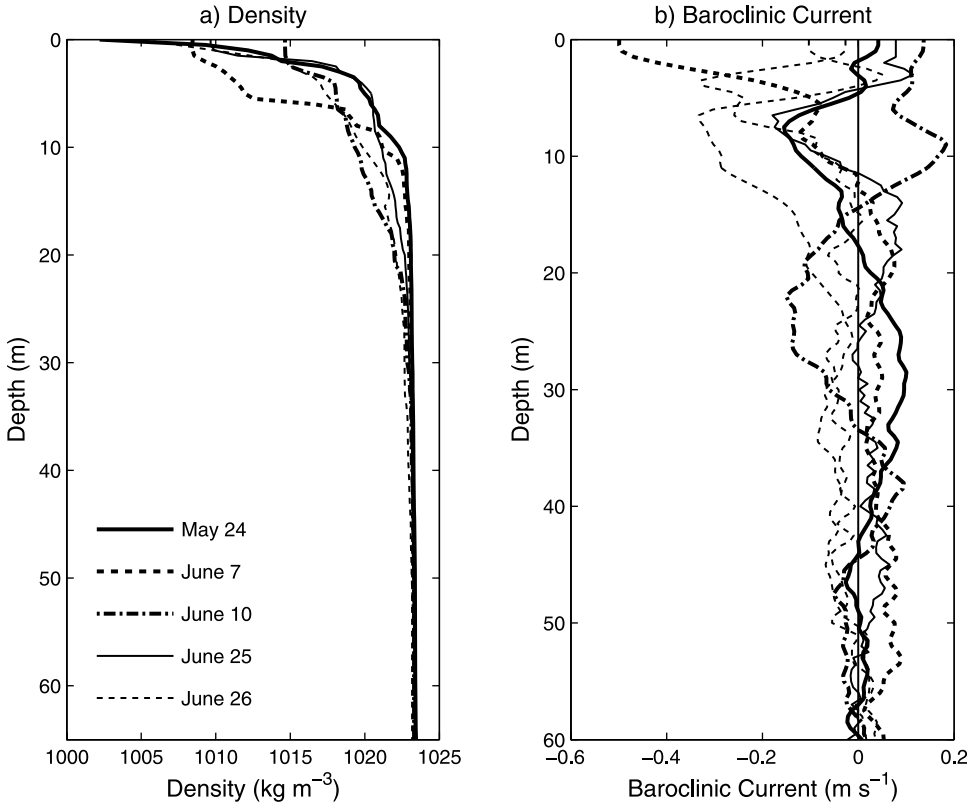

Figure 6. The (a) density profiles and (b) baroclinic currents (taken at times with no internal wave passing by) in the direction of wave propagation for the studied cases of May 24, June 7, June 10, June 25, and June 26. Only the top 60 m are shown. Variations of densities and shear currents are confined in a shallow top layer (about 30 m deep). The rapid density variations are less than 10 m deep. On June 26, data of currents are available for two locations, one location near Point Roberts and another around Active Pass. Positive currents are in the same direction of wave propagation and negative currents are in the opposite direction of wave propagation. The maximum magnitude of the baroclinic currents is less than 0.5 m s^{-1}.

currents this raw data was used, but it was found that wave characteristics computed with vertically smoothed profiles only differed by ≈3%, which is smaller than other uncertainties.

3.3. Wave Phase Speeds

[31] In the processed images (e.g., Figure 3), the rough leading edge of a wave appears darker and the smoother trailing edge is lighter. The northernmost waves in Figure 3 are associated with bands of width less than 100 m and are well-separated (about 200 m apart). It is likely that at least the first five waves are far enough apart that they are no longer interacting. Behind the leading waves is a more confused region about 1 km in extent where wave crests are irregular and the waves are clearly interacting with each other.

[32] One of the most significant benefits of photo imaging is that it allows us to track a particular wave without ambiguity, and calculate its propagation velocity in the direction perpendicular to the wave crest. The phase speeds are taken to be the slope of the least squares fit to wave positions, in the direction perpendicular to wave crests. These waves are also advected by the barotropic tide, and the magnitude of this tidal effect is subtracted to get a true measure of the phase speed relative to the water. Wave phase speed estimation of the wavefront ("1st") in Figure 3 from image sequences is shown in Figure 7 as one example. For each image the location of the leading edge was digitized, and projected onto a vector perpendicular to the wave crests. Their distances are shown in Figure 7 for a 20 minute observation period. The observed offsets are not uniformly increasing in time because of errors associated with the changing observational geometry, but a robust estimation of the propagation speed is obtained by a least squares fit over this time interval. The observed phase speeds range from 0.6 to 1.2 m s^{-1} (Figure 5a), superimposed on tidal currents of less than 0.25 m s^{-1}. The corresponding observed speeds after the tides removed (Figure 5b) have a similar spread.

[33] Generally it appears that larger waves have higher phase speeds (Figure 5b), but the correlation is relatively weak (correlation coefficient is 0.39). In addition to amplitude, many other possible factors can affect the speed of internal waves. Details of the stratification are certainly important, but it is not clear whether or not these details can be usefully simplified into, say, a layered system. Measured shear profiles (Figure 6b) are somewhat difficult to characterize. However, it is not obvious that the shear can be neglected either. These waves, under any reasonable criteria,

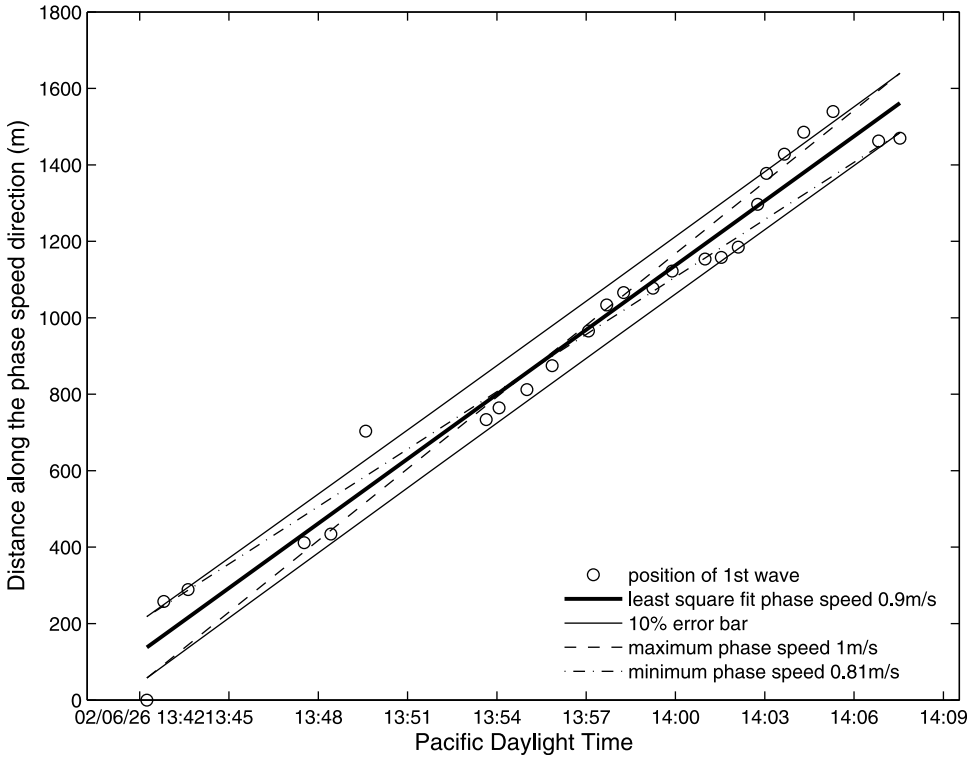

Figure 7. The positions of first wave at different times and its calculated phase speed once the effects of the barotropic tide is subtracted. The time and distances are calculated with the first image in the studied period as the reference.

can be considered "large" in amplitude, since they displace isopycnals at depths of 2–5 m by anywhere from 2 to 7 m.

4. Internal Wave Theory

[34] The wave packets we observed were almost always rank-ordered, with larger well-separated waves at their leading edge. Wave separations are around 4 times of their horizontal length scale. Although these waves are unlikely to represent truly permanent forms they may be similar to solitons and classified as "solitary-like" waves. The mathematical theory of solitary waves, derived under various assumptions, may then be useful as a guide to their behavior. Weakly nonlinear theories can sometimes provide surprisingly accurate predictions, even for waves of large amplitude.

4.1. Internal Solitary Wave Models

[35] One of the most frequently used models of small-amplitude wave propagation is the Korteweg-de Vries (KdV) equation:

$$\eta_t + c_0\eta_x + \alpha\eta\eta_x + \gamma\eta_{xxx} = 0, \tag{1}$$

where η is the vertical layer interface displacement, c_0 is the linear phase speed, α is the nonlinear coefficient, and γ is the dispersion coefficient. It is well-established that nonlinear evolution equations of the KdV type form at least a first-order basis for qualitative modeling and prediction [*Grimshaw*, 1997]. Soliton solutions to this equation take the form of

$$\eta(x,t) = -\eta_0 \mathrm{sech}^2[(x-ct)/L], \tag{2}$$

with phase speed of

$$c = c_0 - \alpha\eta_0/3, \tag{3}$$

and a soliton half width of

$$L = (-12\gamma/\eta_0\alpha)^{1/2}, \tag{4}$$

where $(x - ct)/L$ is the wave phase, and η_0 is the wave amplitude. The crucial parameters α and γ in these equations, which depend on the stratification, shear, and local depth, are described in Appendix A.

[36] Internal solitons in a layered medium have been described by the KdV equation [see, e.g., *Benney*, 1966] since 1876, but the KdV equation applies only to the shallow water ($kD \ll 1$), weakly nonlinear (small but finite amplitude, $\eta_0/D \ll 1$), and weak dispersion ($(D/\lambda)^2 \ll 1$) cases with nonlinearity balancing dispersion. Here η_0 again is a measure of the wave amplitude, $D = h_1 + h_2$ is a measure of water column depth, separated into layers of depth h_1 and h_2, λ is a measure of the wavelength in the direction of wave propagation, and $k = 2\pi/\lambda$. If λ is only long compared to the water depth below or above the interface (e.g., $kh_1 \ll 1$), but not to the whole water depth ($kD > 1$), implying that one of the layers is much thinner than the other, then the waves are called "deep-water" internal waves. For a deep-water wave, small amplitude (weakly nonlinear) internal waves are described by the Benjamin-Ono (BO) equation [*Benjamin*, 1966; *Ono*, 1975]

$$\eta_t + c_0\eta_x + \alpha\eta\eta_x + \gamma\frac{\partial^2}{\partial x^2}\mathcal{H}[\eta] = 0, \tag{5}$$

where the Hilbert operator $\mathcal{H}$ is defined as

$$\mathcal{H}[f] = \frac{1}{\pi}\int_{-\infty}^{+\infty}\frac{f(x')}{x'-x}dx'. \quad (6)$$

and the linear speed c_0 and α and γ are given differently (see Appendix A). Soliton solutions for BO equation are:

$$\eta_{BO}(x,t) = \frac{-\eta_0}{1+((x-ct)/L_{BO})^2}, \quad (7)$$

where

$$L_{BO} = \frac{4\gamma}{\eta_0\alpha}, \quad (8)$$

$$c = c_0 - \alpha\eta_0/4, \quad (9)$$

[37] The weakly nonlinear intermediate-depth case is described by the Intermediate Long Wave equation (ILW) which has been investigated by *Joseph* [1977] and *Kubota et al.* [1978]. The ILW model equation solitons are a family of solutions of one parameter, reducing to either KdV or BO solutions in the appropriate limit.

[38] Unfortunately, the weak nonlinearity (small-amplitude) assumption presumed by KdV, BO, (and ILW) models does not always seem adequate for the experimental and observational data that has been collected by researchers. There are different extended models available such as extended KdV (eKdV) or Gardner equation, containing higher-order nonlinearities for either two-layer or continuously stratified models [*Grimshaw et al.*, 1997; *Michallet and Barthélemy*, 1998]. The eKdV equation has both quadratic and cubic nonlinearities.

[39] An alternative to small-amplitude theories has been numerical solutions of either the fully nonlinear fluid equations or approximations thereof [e.g., *Green and Naghdi*, 1977; *Lamb and Yan*, 1996; *Choi and Camassa*, 1999; *Vlasenko et al.*, 2000]. The fully nonlinear models are usually restricted to steady state, otherwise, the calculation of time-dependent solutions can be computationally expensive [*Helfrich and Melville*, 2006]. Another alternative are analytical theories for waves of maximal amplitude [*Choi and Camassa*, 1999].

[40] Note that for the waves we observe, $D \approx 120$ m, $h_1 =$ 2–5 m, $\eta_0 =$ 2–7 m, and $\lambda \approx 50$ m. Thus $kD \approx 15$, $\eta_0/D \sim O(0.01)$, and $\eta_0/h_1 \sim O(1)$. Thus we would expect these to be deep water, large, nonlinear internal waves. They are, however, far from maximal in amplitude [*Wang*, 2009]. However, among all the models or equations, the KdV model seems to have the widest application in successful prediction of experimental or observational solitons, even for large amplitude solitary-like waves which are outside of the strict assumption of the KdV theory, while BO or ILW theory appears not to do so [e.g., *Grue et al.*, 1999; *Koop and Butler*, 1981; *Small et al.*, 1999]. "The question of why this solution is suitable for waves of such large amplitude remains open" [*Small et al.*, 1999]. Some laboratory results [e.g., *Koop and Butler*, 1981] even suggest that the KdV model matches observations better in deep water than the BO theory which was specifically designed for such cases. *Koop and Butler* [1981] as in the review by *Ostrovsky and Stepanyants* [2005] show a better match in a laboratory situation for wavelengths in deep water with KdV models. Some observational research has also shown that the KdV equation is quite reasonable in deep water, at least when wave amplitudes and particle velocities are compared [e.g., *Osborne and Burch*, 1980], but a definitive comparison has not yet been carried out.

[41] In addition to the uncertainty about which basic approach will work best in a particular situation, additional uncertainty arises when we attempt to compute the α and γ parameters for the different equations. These require additional assumptions about the nature of the stratification and the background shear.

4.2. Internal Solitary Waves in Background Shear

[42] Shear is often ignored in studies of nonlinear waves. However, *Holloway et al.* [1997] used a generalized KdV equation to investigate the effect of shear and obtained numerical solutions. They found that for the cases they considered, the phase speed could be affected by shear by as much as 15% to 30%. *Grimshaw* [1998] and *Tung et al.* [1981] also studied the effect of shear on nonlinear internal waves and pointed out that a horizontal background shear modified the wave parameters including wave phase speed and wave half width. *Stastna and Lamb* [2002] studied the effect of background shear on large fully nonlinear internal solitary waves under continuous stratification and claimed that the presence of a background current could also affect the maximal wave amplitude by modifying the wave breaking onset condition. *Choi* [2006] considered a two-layer system (x-z plane) with uniform shear and obtained an analytical solution of his strongly nonlinear model with a Boussinesq assumption. He found, when compared with the irrotational (no shear) case, that positive vorticity slowed down the propagation and increased the width of a wave of depression propagating in the positive x-direction while it sped up the propagation and decreased the wave width if the depression was propagating in the negative x-direction.

[43] The existing literature thus suggests that if there is discrepancy between observation and model prediction, an important factor which deserves attention is the effect of the background shear or equivalently of baroclinic currents. On the other hand, extending weakly nonlinear theories to include shear effects can be done in a straightforward manner because if a wave of fixed amplitude satisfies the KdV (or other related) equations in the absence of shear, it will also do this in the presence of shear, with only the equation coefficients being modified [*Grimshaw*, 1998]. Other papers that discuss the shear effect on continuously stratified internal waves include those by *Tung et al.* [1981] and *Maslowe and Redekopp* [1980].

[44] Here, the effect of shear is examined by including/excluding baroclinic currents in different internal wave theories to predict wave propagation speeds. Comparisons are made with the observed values. Two-layer cases are analyzed before the more complicated continuously stratified cases.

5. Analysis

5.1. Two-Layer Stratified Cases

[45] A two-layer approximation is often used for its analytical simplicity and therefore it makes sense to begin with

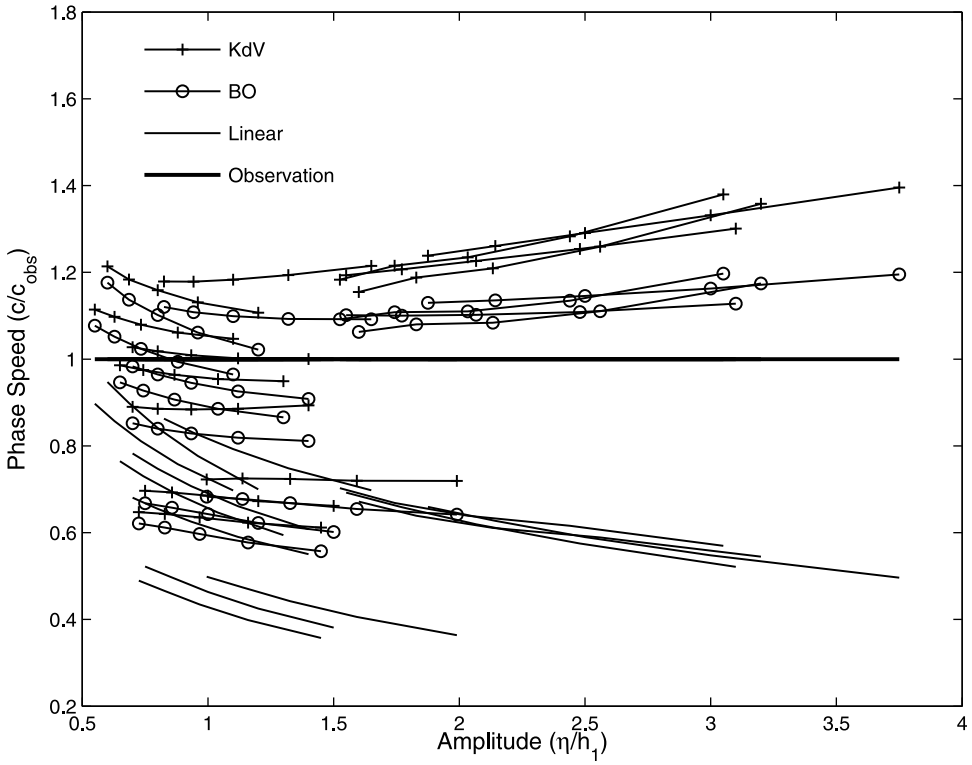

Figure 8. Comparison of wave speeds predicted by two-layer theories (KdV, BO, linear) with observed values. For each case, the wave amplitude is fixed as the observed value for that wave (i.e., from Figure 5) and the upper layer depth h_1 varied between 2 and 4 m. The left end of each line corresponds to an upper layer depth of 4 m and the right end corresponds to an upper layer depth of 2 m. The vertical axis is model predicted phase speed relative to the corresponding observed wave phase speeds, c/c_{obs}. The horizontal axis is the normalized wave amplitude.

this approximation. However, it is not obvious how one would precisely define such an approximation for the types of density profiles observed here (Figure 6). Heuristically, an "upper layer depth", however defined, would likely be no larger than a few meters. Rather than fix this depth at any particular value, we shall investigate the sensitivity of the results over a range of choices, to see whether reasonable results can be obtained by a tuning procedure. A sequence of layer depths is chosen a priori over the range of 2 to 4 m. Densities and background baroclinic velocities are then averaged above and below this layer depth.

[46] We then calculate the predicted phase speeds from linear long-wave theory, as well as from different nonlinear theories, all using the two-layer approximation (Figure 8). For all the studied cases, the BO equation predictions are very similar to eKdV, strongly nonlinear and ILW equation predictions. Thus the results for eKdV, strongly nonlinear, and ILW equations are not shown in Figure 8. The horizontal axis is a nondimensional wave amplitude formed by dividing the measured amplitude by the (varying) upper layer depth and the vertical axis is the ratio of the predicted wave phase speed to the corresponding observed wave phase speed. Ideally we could have $c/c_{obs} = 1$ for some η/h_1. Values for each wave then appear along a roughly horizontal line, with the numerical values for shallowest choice of layer depth at the right-hand end.

[47] The results (Figure 8) of this procedure are not exactly the same for different cases, but some qualitative conclusions can be made. First of all, it is clear that none of the two-layer model equations can be chosen with confidence to predict the propagation of the studied waves. In no case do the predictions collapse onto $c/c_{obs} = 1$, whatever layer depth is chosen. In fact, the sensitivity to layer depth is relatively weak, with most of the curves lying roughly horizontally, and scattered above and below $c/c_{obs} = 1$. Also, whereas c/c_{obs} for linear predictions tends to be less than 1 (i.e. underpredicts the wave speed), c/c_{obs} for various nonlinear models is much higher. Values are of the right order for agreement, although there is still a great deal of scatter about 1 for individual cases. Although it is not clear which of the weakly nonlinear and strongly nonlinear equations studied best describes the propagation speeds of the studied waves, it is rather obvious that the linear predictions are generally lower than the observed values.

[48] The similarity between solutions to the BO, eKdV, strongly nonlinear, and ILW equations suggests that the degree of nonlinearity is not an important factor in predictions of wave speed, and that the range of depths is not particularly problematic either, with the "deep water" approximation remaining valid. Due to similarity to the BO predictions, results for eKdV, strongly nonlinear, and ILW equations are not explicitly included in the study of continuous cases.

5.2. Continuously Stratified Cases

[49] If we move from a layered approximation to a continuous stratification, expressions for the α and γ coefficients

now involve integrals over complex functions involving mode shapes derived from the Taylor-Goldstein equation (Appendix A), but these can be evaluated numerically using our observed stratification and shear profiles.

[50] The results of fitting to weakly nonlinear model equations with continuous stratification are summarized in Figure 9. The results are displayed in six panels. The three panels (a, c, and e) on the left-hand side compare predictions neglecting baroclinicity with observations. The three panels (b, d, and f) on the right-hand side show the corresponding comparisons once baroclinic effects are included. Uncertainties in observed propagation speeds are given by horizontal error bars, and in predicted quantities (mostly a function of uncertainty in amplitude) by vertical error bars. These vertical error bars do not have a formal statistical meaning, but rather represent the propagation of our "best estimates" of the error in the observations. In general, the observed wave speeds are between 0.7 m s^{-1} and 1.1 m s^{-1} with error bars less than 0.1 m s^{-1} and the predicted speeds are between 0.6 m s^{-1} and 1.1 m s^{-1} with error bars less than 0.1 m s^{-1} as well. The thirteen cases are widely scattered around the 1:1 line except panel f).

[51] By comparing the three panels on the left-hand side with the three on the right-hand side, it is evident shear significantly affects wave speeds. First consider the linear cases in the top two panels a) and b). Before the shear currents are included, predictions are smaller than observations for all cases except two waves on June 7. After shear is included, predictions are smaller than observations for all cases, albeit more tightly grouped. For all cases, the linear equation tends to underestimate the observed propagation speeds with the predicted wave speeds between 0.6 m s^{-1} and 0.9 m s^{-1}.

[52] The KdV predicted wave speeds (panels c and d) are generally faster than the linear equation predictions with predictions ranging between 0.7 m s^{-1} and 1.0 m s^{-1}. The comparison between predictions and observations are better than the linear cases, but there is still much scatter. Most predictions are still several error bars different than observations.

[53] Finally consider the bottom two panels (e and f) for the BO equation. Comparing the sheared BO (f) with the sheared KdV (d) predictions, some of the markers are further moved upward and some are moved downward. The BO equation predicts phase speeds that are different from those of the KdV equation. For 11 of the 13 cases the BO predictions, with baroclinicity included, overlap with observations within the error bars, and the 2 remaining cases are very close.

[54] Without including the effects of shear currents, none of the classic models are particularly satisfactory. For most cases, the difference between the predicted values and the observed values are much greater than the error bars. Matching between the BO equation predictions and observations are not obviously better than the matching between KdV predictions and observations. However, after the effects of shear are included, the matching between the BO equation predictions and observations are greatly improved and the BO predictions are overall closer to observations than KdV predictions. Including shear significantly improves predictions for KdV and BO models in the sense of matching with observations, but only the BO equation can predict wave propagation within the observational uncertainties.

6. Conclusion and Discussion

[55] By using photogrammetrically rectified sequences of oblique aerial photographs, relatively precise measurements have been made of wave propagation speeds in a variety of conditions in the Strait of Georgia. Not only were particular waves unambiguously identified over the length of the sequences, but we could choose waves in a packet that were far enough apart that they could reasonably be described as "solitary-like" and compared with known soliton solutions. Wave propagation speeds and directions are determined using oblique aerial photography. Wave propagation directions may also be estimated by analysis of the spatially-separated beams of a moored ADCP [*Chang et al.*, 2010]. Measured propagation speeds were between 0.6 and 1.2 m s^{-1}. Particular attention was paid to quantifying the measurement errors, which were typically about 10%. Previous attempts at verifying wave theories have relied on comparisons with the waveshape and particle velocities.

[56] In addition, simultaneous water column measurements of stratification and water column velocity allowed us to both determine wave amplitudes, as well as background conditions and tidal effects. Wave amplitudes ranged from 2 to over 7 m. Correction for tidal effects was important. The magnitude of the tidal current was between 0.02 and 0.25 m s^{-1}.

[57] The largest changes in stratification occurred very near the surface, such that a reasonable "layer depth" of the upper layer would be only a few meters, in a water column >120 m in depth. The internal waves are thus "large" in the sense that a scaling of $\eta/h_1 \geq O(1)$, but fall well within a "deep water" classification. Weakly nonlinear internal waves are described by classic model equations and in particular their results are often arbitrarily applied in strongly nonlinear cases, such as those we observe here. Most laboratory or field research surveys in the literature match observations against the shallow-water KdV equation, even when their waves are strictly out of the scope of the KdV equation because they are in deep-water regime [*Osborne and Burch*, 1980; *Koop and Butler*, 1981; *Michallet and Barthélemy*, 1998] or have large-amplitudes [*Small et al.*, 1999].

[58] Our investigations showed that the weakly nonlinear BO equations, using continuous stratification and including shear effects, correctly predicted wave propagation speeds. In fact there was little difference in predicted speeds between the weakly nonlinear two-layer BO and a fully nonlinear two-layer prediction, suggesting that extending the theoretical descriptions to include higher order nonlinearities is not important in modeling real oceanic internal waves. This is the first time that a BO description has been found to usefully model a real-world situation.

[59] On the other hand, two-layer approximations were inadequate, even when tuning of the layer depths was attempted. The fact that continuously stratified equations provide better predictions than two-layer approximations was previously found to be true in a situation where the KdV equation provided the best description [*Gan and Ingram*, 1992].

[60] Also, although baroclinic velocities were small and not easily related to the density field, their effect was important. Before the baroclinic currents (i.e. shear effects)

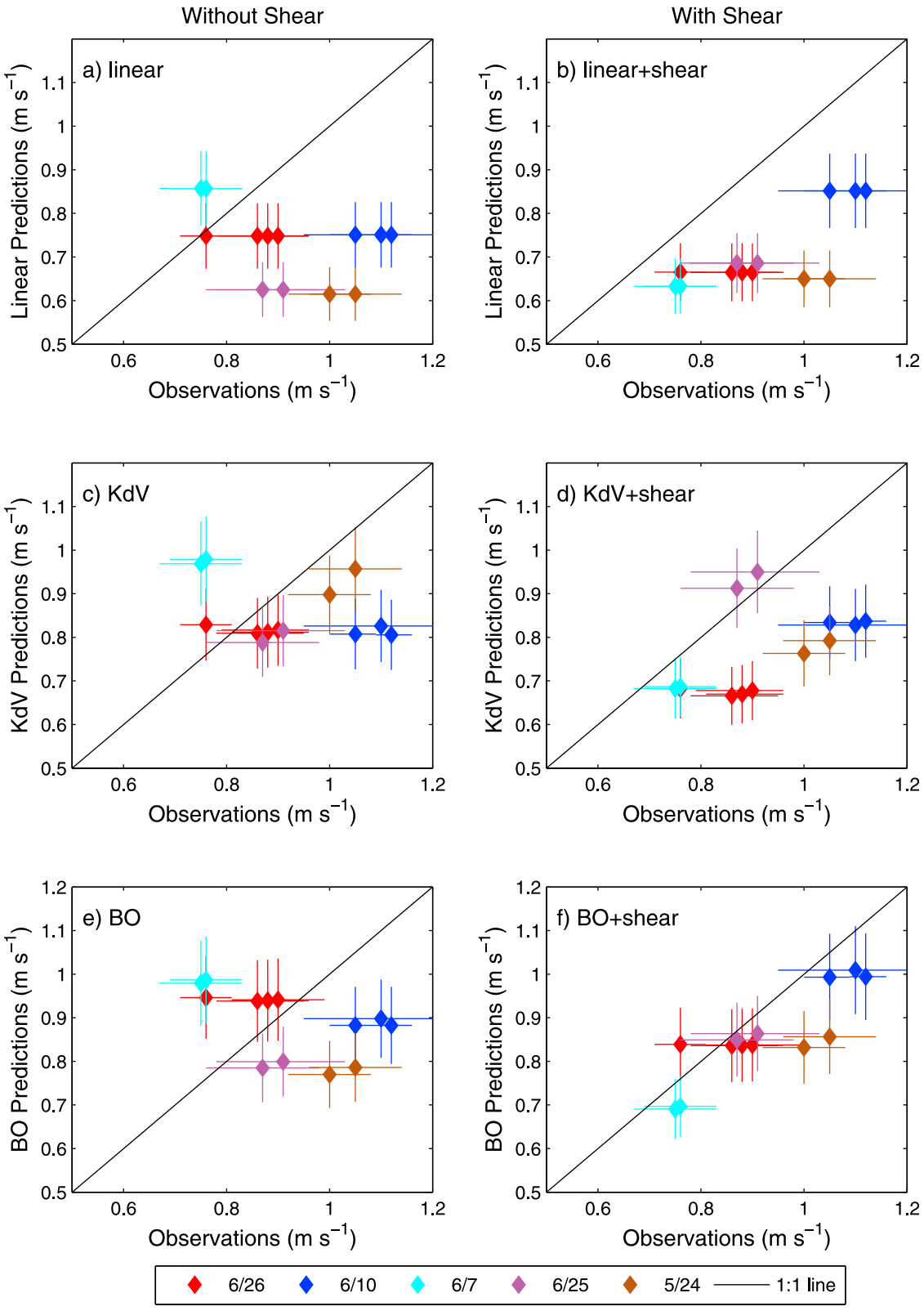

Figure 9. Comparison between observed and predicted wave propagation speeds using continuous models. There are thirteen wave cases from five different days. The vertical line crossing each dot is the error bar due to wave amplitude estimation. The horizontal line is the error bar coming from wave phase speed estimation.

were included, none of the studied model equations, including the BO equation, could provide satisfactory predictions of propagation speeds. The effect of shear is evident in all cases for all the different predictions. If the surface baroclinic current is in the same direction as the wave propagation, the predicted phase speeds in all situations are increased. When the upper layer baroclinic current is negative, they are all decreased. Largest velocities were somewhat smaller than wave propagation speeds, so the formation of critical layers was not important.

[61] Our situation is somewhat different from *Choi* [2006] who studied the effect of shear numerically. *Choi*'s model has uniform linear shear slope in both the upper layer and the lower layer, while for our cases, the lower layer is rather quiet with nearly no stratification and zero baroclinic current or shear slope. However, if we substitute $\Omega_2 = 0$ (zero lower layer shear) or $\Omega_2 \ll \Omega_1$ into Choi's equation (2.9), positive Ω_1 (positive upper layer baroclinic current) will increase the wave propagation speed in the positive x-direction, i.e. the upper layer baroclinic current direction, which is what we expect based on our observations above.

[62] We have neglected to consider the effects of the earth's rotation in our analysis. The effect of Coriolis terms has been investigated in the study of internal waves [e.g., *Gilman et al.*, 1996; *Helfrich*, 2007; *Helfrich and Grimshaw*, 2008; *Helfrich*, 2008; *Farmer et al.*, 2009]. Rotation is found to have some effect, especially when the length scales of internal waves are of the order of tens of kilometers or of the scale of internal tides [*Gilman et al.*, 1996; *Helfrich*, 2008]. These scales are much larger than those considered in our observations. However, according to *Helfrich* [2007], when the length scale (l) is smaller than the deformation radius, the effect of rotation is still not necessarily negligible. If $\gamma^2 = O(\alpha)$ (where $\gamma = l/L_R$, $\alpha = a/h_s$, a is amplitude, h_s is the characteristic depth scale, L_R is the deformation radius) then these weak rotational effects are comparable to the nonlinear and nonhydrostatic effects. For the waves observed in the Strait of Georgia, l is about 50 m, and L_R is about 30 km, therefore $\gamma = O(10^{-3})$, while $\alpha = O(1)$. Thus, $\gamma^2 \ll O(\alpha)$, and so the rotational effect is small. The relative importance of rotation compared to nonlinear and nonhydrostatic terms can also be estimated using the Ostrovsky equation (a KdV equation with rotation) [*Farmer et al.*, 2009]. The Ostrovsky number, a ratio of the nonlinear to rotational terms is calculated as $O_s = O(10^3)$ for waves observed in the Strait of Georgia. The ratio of the nonhydrostatic term to rotational term is calculated as ≈600. It is clear that rotational effects are very small compared to nonlinear and nonhydrostatic effects. Finally, individual waves were tracked for less than an hour, far less than an inertial period. Thus, even if these small rotational effects have long-term consequences, they are unlikely to appear in our data set. It is possible that rotation may play a role in the large-scale degeneration of internal tides into these smaller waves, but in the Strait of Georgia it is more likely that these waves are initially formed by the tidal release of topographic lee waves less than 12 hours earlier [*Wang*, 2009].

[63] Finally, it is perhaps unexpected that the propagation speeds of these strongly nonlinear large-amplitude internal waves in the Strait of Georgia are reasonably well described by weakly nonlinear deep-water theory (with continuous stratification and shear) even though their amplitudes are $O(1)$. However, this conclusion, derived from geophysical observations, is also supported by a recent numerical analysis. *Camassa et al.* [2006] compared a strongly nonlinear model with weakly nonlinear KdV and ILW theory in a two-layer system. In Camassa et al.'s Figures 14a and 15a, when the wave amplitude is about 1 or less, the weakly nonlinear theory is not dramatically different from the fully nonlinear theory or the experimental data collected by *Michallet and Barthélemy* [1998]. Of course the difference between the weakly nonlinear theories and the strongly nonlinear theory and the difference between theories and the experimental data increases with the increase of the wave amplitude. Based on their results, if the wave amplitudes in the Strait of Georgia became significantly greater than 1, we may find that no weakly nonlinear theory is able to describe the waves. Interestingly, *Camassa et al.* [2006], like most of other existing literature, found that KdV theory works better than a deep-water configuration (called ILW in their paper) even in deep-water situations. The lack of success of previous research in using the BO model is likely because shear and stratification effects are not correctly accounted for, rather than any shortcoming of the BO model itself.

Appendix A

[64] Parameters for two-layer KdV equation are:

$$c_0 = \left[g(\Delta\rho/\rho)h_{eff}\right]^{1/2}, \tag{A1}$$

$$\alpha = -(3c_0/2)\frac{h_2 - h_1}{h_1 h_2}, \tag{A2}$$

$$\gamma = c_0 h_1 h_2/6, \tag{A3}$$

where $h_{eff} = h_1\ h_2/(h_1 + h_2)$, and h_1 and h_2 represent the depths of the upper and lower layers.

[65] Parameters for two-layer BO equation:

$$c_0 = [g(\Delta\rho/\rho)h_1]^{1/2}, \tag{A4}$$

$$\alpha = -\frac{3c_0}{2h_1}, \tag{A5}$$

$$\gamma = \frac{c_0\rho_2 h_1}{2\rho_1}, \tag{A6}$$

[66] In a continuously stratified and sheared system, the KdV equation (1) and its solutions (2)–(4) still apply, but its coefficients are now dependent on the mode shape (ϕ) and mode speed (c_{shear}) of the linear long wave Taylor-Goldstein (TG) equation (A7) with wave number $k = 0$.

[67] The Taylor-Goldstein (TG) equation can be written [*Baines*, 1995]:

$$\frac{d^2}{dz^2}\phi + \left[\frac{N^2}{(U - c_{shear})^2} - \frac{U_{zz}}{U - c_{shear}}\right]\phi - k^2\phi = 0. \tag{A7}$$

with boundary conditions:
at $z = 0$,

$$\phi = 0, \tag{A8}$$

at $z = -D$,

$$\phi = 0, \tag{A9}$$

where ϕ is mode shape, k is wave number, $U(z)$ is the baroclinic current, c_{shear} is the linear wave phase speed with baroclinic current U, $N = \sqrt{-(g/\rho)(\partial\rho/\partial z)}$ is the buoyancy frequency.

[68] In solution (3) c_0 is now replaced with the mode speed c_{shear} of equation (A7) and α and γ are given by [*Grimshaw*, 1998; *Stastna and Lamb*, 2002]:

$$\alpha = \frac{3}{2}\int_{-D}^{0} \rho_0 (c_{shear} - U)^2 \psi_z^3 dz / I, \tag{A10}$$

$$\gamma = \frac{1}{2}\int_{-D}^{0} \rho_0 (c_{shear} - U)^2 \psi^2 dz / I, \tag{A11}$$

where

$$I = \int_{-D}^{0} \rho_0 (c_{shear} - U) \psi_z^2 dz, \tag{A12}$$

with $\psi = \phi/(c_{shear} - U)$ and $\psi_z = d\psi/dz$.

[69] For the BO equation, since the internal waves observed in the Strait of Georgia have wavelengths much greater than the depth of the thin layer where density stratification and baroclinic currents reside, these internal waves can be treated as long waves inside the thin shear layer (with depth h_1), and then asymptotically matched to a short wave solution in an infinitely deep lower layer with uniform density and no shear. The profiles are then used in the Taylor-Goldstein equation to get mode shape (ϕ) and mode speed (c_{shear}) [*Grimshaw*, 1998; *Tung et al.*, 1981; *Maslowe and Redekopp*, 1980]. The boundary conditions are rigid top and zero derivatives at the virtual boundary at infinity ($\phi_z = 0$ at $z = -\infty$) in the asymptotic upper layer solution. With this mode shape and mode speed, α is again given by equations (A10) and (A12) with $-D$ now replaced by $-\infty$. The parameter γ is given by $I\gamma = (\rho_0 c_0^2 \psi^2)_{z\to\infty}$ according to *Grimshaw* [1998]. The lower boundary is taken to be at −500 m for numerical convenience, changing to −1000 m makes little difference.

[70] Below the shear layer, the wave is not "long" any longer, therefore the term $-k^2\phi$ in the TG equation needs to be considered. Also stratification and currents below the shear layer will be uniform, which means that the shear and the buoyancy frequency will both be zero. Then the equation for this outside domain is a solution to $(d^2\phi/dz^2) - k^2\phi = 0$, and the outside region solution has to match with the inside solution of the shear layer. The solution of this outside domain then is $\phi = Ae^{-kz}$, which will need to be normalized so that its maximum is 1 in order to match the wave modes of the inside waveguide domain.

[71] **Acknowledgments.** We wish to thank the crew of the CCGS *Siyay* for their outstanding assistance in helping us hang instruments off all parts of the vessel. This research was supported by the Natural Sciences and Engineering Research Council of Canada under grant 194270-02. This research was also partially supported by the National Natural Science Foundation of China under grant 41106008.

References

Apel, J. R., L. A. Ostrovsky, and Y. A. Stepanyants (1995), Internal solitons in the ocean, *Rep. MERCJRA0695*, Johns Hopkins Univ. Appl. Phys. Lab., Baltimore, Md.

Baines, P. G. (1995), *Topographic Effects in Stratified Flows*, Cambridge Univ. Press, New York.

Benjamin, T. B. (1966), Internal waves of finite amplitude and permanent form, *J. Fluid Mech.*, *25*, 241–270, doi:10.1017/S0022112066001630.

Benney, D. J. (1966), Long non-linear waves in fluid flows, *J. Math. Phys.*, *45*, 52–63.

Bourgault, D. (2007), Shore-based photogrammetry of river ice, *Can. J. Civ. Eng.*, *35*(1), 80–86, doi:10.1139/L07-087.

Camassa, R., W. Choi, H. Michallet, P.-O. Rusas, and J. K. Sveen (2006), On the realm of validity of strongly nonlinear asymptotic approximations for internal waves, *J. Fluid Mech.*, *549*, 1–23, doi:10.1017/S0022112005007226.

Centurioni, L. R. (2010), Observations of large-amplitude nonlinear internal waves from a drifting array: Instruments and methods, *J. Atmos. Oceanic Technol.*, *27*, 1711–1731, doi:10.1175/2010JTECHO774.1.

Chang, M.-H., R.-C. Lien, Y. J. Yang, and T. Y. Tang (2010), Nonlinear internal wave properties estimated with moored ADCP measurements, *J. Atmos. Oceanic Technol.*, *28*, 802–815, doi:10.1175/2010JTECHO814.1.

Choi, W. (2006), The effect of a background shear current on large amplitude internal solitary waves, *Phys. Fluids*, *18*, 1–7, doi:10.1063/1.2180291.

Choi, W., and R. Camassa (1999), Fully nonlinear internal waves in two-fluid system, *J. Fluid Mech.*, *396*, 1–36, doi:10.1017/S0022112099005820.

Colosi, J. A., R. C. Beardsley, J. F. Lynch, G. Gawarkiewicz, C.-S. Chiu, and A. Scotti (2001), Observations of nonlinear internal waves on the outer New England continental shelf during the summer Shelfbreak Primer study, *J. Geophys. Res.*, *106*(C5), 9587–9601, doi:10.1029/2000JC900124.

Cummins, P., S. Vagle, L. Armi, and D. Farmer (2003), Stratified flow over topography: Upstream influence and generation of nonlinear internal waves, *Proc. R. Soc. London, Ser. A*, *459*, 1467–1487, doi:10.1098/rspa.2002.1077.

D'Asaro, E. A. (2003), Performance of autonomous Lagrangian floats, *J. Atmos. Oceanic Technol.*, *20*, 896–911.

Dushaw, B. D., B. D. Cornuelle, P. F. Worcester, B. M. Howe, and D. S. Luther (1995), Barotropic and baroclinic tides in the central North Pacific Ocean determined from long-range reciprocal acoustic transmissions, *J. Phys. Oceanogr.*, *25*, 631–647.

Farmer, D., and L. Armi (1999), Stratified flow over topography: The role of small-scale entrainment and mixing in flow establishment, *Proc. R. Soc. London, Ser. A*, *455*, 3221–3258, doi:10.1098/rspa.1999.0448.

Farmer, D., Q. Li, and J. Park (2009), Internal wave observations in the South China Sea: The role of rotation and non-linearity, *Atmos. Ocean*, *47*(4), 267–280, doi:10.3137/OC313.2009.

Foreman, M. G. G., R. A. Walters, R. F. Henry, C. P. Keller, and A. G. Dolling (1995), A tidal model for eastern Juan de Fuca Strait and the southern Strait of Georgia, *J. Geophys. Res.*, *100*(C1), 721–740, doi:10.1029/94JC02721.

Gan, J., and R. G. Ingram (1992), Internal hydraulics, solitons and associated mixing in a stratified sound, *J. Geophys. Res.*, *97*(C6), 9669–9688, doi:10.1029/92JC00491.

Gargett, A. E. (1976), Generation of internal waves in the Strait of Georgia, British Columbia, *Deep Sea Res.*, *23*(1), 17–20, doi:10.1016/0011-7471(76)90805-6.

Gargett, A. E., and B. A. Hughes (1972), On the interaction of surface waves and internal waves, *J. Fluid Mech.*, *52*(1), 179–191, doi:10.1017/S0022112072003027.

Gilman, O. A., R. Grimshaw, and Y. A. Stepanyants (1996), Dynamics of internal solitary waves in a rotating fluid, *Dyn. Atmos. Oceans*, *23*, 403–411.

Green, A. E., and P. M. Naghdi (1977), Water waves in a nonhomogeneous incompressible fluid, *J. Applied Mech.*, *44*(4), 523–528, doi:10.1115/1.3424129.

Grimshaw, R. (1997), Internal solitary waves, in *Advances in Coastal and Ocean Engineering*, vol. 3, edited by P. L.-F. Liu, pp. 1–30, World Sci., Singapore.

Grimshaw, R. (1998), Internal solitary waves in shallow seas and lakes, in *Physical Processes in Lakes and Oceans*, *Coastal Estuarine Stud.*, vol. 54, edited by J. Imberger, pp. 227–240, AGU, Washington, D. C.

Grimshaw, R., E. Pelinovsky, and T. Talipova (1997), The modified Korteweg-de Vries equation in the theory of large-amplitude internal waves, *Nonlinear Processes Geophys.*, *4*, 237–250, doi:10.5194/npg-4-237-1997.

Grue, J., A. Jensen, P. Rusas, and J. Sveen (1999), Properties of large-amplitude internal waves, *J. Fluid Mech.*, *380*, 257–278, doi:10.1017/S0022112098003528.

Halverson, M. J., and R. Pawlowicz (2008), Estuarine forcing of a river plume by river flow and tides, *J. Geophys. Res.*, *113*, C09033, doi:10.1029/2008JC004844.

Helfrich, K. (2007), Decay and return of internal solitary waves with rotation, *Phys. Fluids*, *19*, 026601, doi:10.1063/1.2472509.

Helfrich, K. (2008), Continuously stratified nonlinear low-mode internal tides, *J. Mar. Res.*, *66*(3), 299–323.

Helfrich, K., and R. Grimshaw (2008), Nonlinear disintegration of the internal tide, *J. Phys. Oceanogr.*, *38*, 686–701, doi:10.1175/2007JPO3826.1.

Helfrich, K., and W. Melville (2006), Long nonlinear internal waves, *Annu. Rev. Fluid Mech.*, *38*, 395–425.

Holloway, P., E. Pelinovsky, T. Talipova, and B. Barnes (1997), A nonlinear model of internal tide transformation on the Australian North West Shelf, *J. Phys. Oceanogr.*, *27*, 871–896.

Hughes, B. A., and R. F. Gasparovic (1988), Introduction, *J. Geophys. Res.*, *93*(C10), 12217, doi:10.1029/JC093iC10p12217.

Joseph, R. J. (1977), Solitary waves in finite depth fluid, *J. Phys. A Math. Gen.*, *10*, L225–L227.

Klymak, J. M., and M. C. Gregg (2004), Tidally generated turbulence over the Knight Inlet Sill, *J. Phys. Oceanogr.*, *34*, 1135–1151.

Koop, C. G., and G. Butler (1981), An investigation of internal solitary waves in a two-fluid system, *J. Fluid Mech.*, *112*, 225–251, doi:10.1017/S0022112081000372.

Kubota, T., D. R. S. Ko, and L. D. Dobbs (1978), Weakly-nonlinear, long internal gravity waves in stratified fluids of finite depth, *J. Hydronautics*, *12*, 157–165.

Lamb, K. G., and L. Yan (1996), The evolution of internal wave undular bores: Comparison of a fully nonlinear numerical model with weakly nonlinear theory, *J. Phys. Oceanogr.*, *26*, 2712–2734.

LeBlond, P. H., and L. A. Mysak (1978), *Waves in the Ocean*, *Elsevier Oceanogr. Ser.*, vol. 20, Elsevier Sci., Amsterdam.

Li, Q., D. M. Farmer, T. F. Duda, and S. R. Ramp (2009), Acoustic measurement of nonlinear internal waves using the inverted echo sounder, *J. Atmos. Oceanic Technol.*, *26*, 2228–2242.

Marmorino, G. O. (1987), Observations of small-scale mixing processes in the seasonal thermocline, Part II: Wave breaking, *J. Phys. Oceanogr.*, *17*, 1348–1355.

Maslowe, S., and L. Redekopp (1980), Long nonlinear waves in stratified shear flows, *J. Fluid Mech.*, *101*, 321–348, doi:10.1017/S0022112080001681.

Michallet, H., and E. Barthélemy (1998), Experimental study of interfacial solitary waves, *J. Fluid Mech.*, *366*, 159–177, doi:10.1017/S002211209800127X.

Moum, J. N., D. M. Farmer, W. D. Smyth, K. Armi, and S. Vagle (2003), Structure and generation of turbulence at interfaces by internal solitary waves propagating shoreward over the continental shelf, *J. Phys. Oceanogr.*, *33*, 2093–2112.

Ono, H. (1975), Algebraic solitary waves in stratified fluids, *J. Phys. Soc. Jpn.*, *39*, 1082–1091.

Osborne, A. R., and T. L. Burch (1980), Internal solitons in the Andaman Sea, *Science*, *208*, 451–460, doi:10.1126/science.208.4443.451.

Ostrovsky, L. A., and A. Stepanyants (2005), Internal solitons in laboratary experiments: Comparison with theoretical models, *Chaos*, *15*, 037111.

Pawlowicz, R. (2003), Quantitative visualization of geophysical flows using low-cost oblique digital time-lapse imaging, *IEEE J. Oceanic Eng.*, *28*(4), 699–710, doi:10.1109/JOE.2003.819310.

Pawlowicz, R., O. Riche, and M. Halverson (2007), The circulation and residence time of the Strait of Georgia using a simple mixing-box approach, *Atmos. Ocean*, *45*(2), 173–193.

Pinkel, R. (1983), Doppler sonar observations of internal waves, wave-field structure, *J. Phys. Oceanogr.*, *13*, 804–815.

Pinkel, R., M. A. Goldin, J. A. Smith, O. M. Sun, A. A. Aja, M. N. Bui, and T. Hughen (2011), The wirewalker: A vertically profiling instrument carrier powered by ocean waves, *J. Atmos. Oceanic Technol.*, *28*, 426–435.

Ramp, S. R., T. Y. Tang, T. F. Duda, J. F. Lynch, A. K. Liu, C. S. Chiu, F. L. Bahr, H. R. Kim, and Y. J. Yang (2004), Internal solitons in the Northeastern South China Sea. Part I: Sources and deep water propagation, *IEEE J. Oceanic Eng.*, *29*(4), 1157–1180.

Shand, J. A. (1953), Internal waves in Georgia Strait, *Trans. AGU*, *34*(6), 849–856.

Small, J., Z. Hallock, G. Pavey, and J. Scott (1999), Observations of large amplitude internal waves at the Malin shelf-edge during SESAME 1995, *Cont. Shelf Res.*, *19*, 1389–1436, doi:10.1016/S0278-4343(99)00023-0.

Stastna, M., and K. Lamb (2002), Large fully nonlinear internal solitary waves: The effect of background currents, *Phys. Fluids*, *14*, 2987–2999, doi:10.1063/1.1496510.

Tedford, E. W., J. R. Carpenter, R. Pawlowicz, R. Pieters, and G. A. Lawrence (2009), Observation and analysis of shear instability in the Fraser River estuary, *J. Geophys. Res.*, *114*, C11006, doi:10.1029/2009JC005313.

Tung, K., D. Ko, and J. Chang (1981), Weakly nonlinear internal waves in shear, *Stud. Appl. Math.*, *65*, 189–221.

Turner, J. S. (1973), *Buoyancy Effects in Fluids*, Cambridge Univ. Press, Cambridge, U. K.

van Haren, H. (2005), Details of stratification in a sloping bottom boundary layer of Great Meteor Seamount, *Geophys. Res. Lett.*, *32*, L07606, doi:10.1029/2004GL022298.

Vlasenko, V., P. Brandt, and A. Rubino (2000), Structure of large-amplitude internal solitary waves, *J. Phys. Oceanogr.*, *30*, 2171–2185.

Wang, C. (2009), Geophysical observations of nonlinear internal solitary-like waves in the Strait of Georgia, Ph.D. thesis, Univ. of B. C., Vancouver, Canada.

Wijffels, S., and G. Meyers (2004), An intersection of oceanic waveguides: Variability in the Indonesian throughflow region, *J. Phys. Oceanogr.*, *34*, 1232–1253.

R. Pawlowicz, Department of Earth and Ocean Sciences, University of British Columbia, 6311 Stores Rd., Vancouver, BC V6T 1Z1, Canada.

C. Wang, Physical Oceanography Laboratory, Ocean University of China, 238 Songling Rd., Qingdao, 266100 China. (cxwang@ouc.edu.cn)